



**HAL**  
open science

## Solid state chemistry for developing better metal-ion batteries

Artem M Abakumov, Stanislav S Fedotov, Evgeny V Antipov, Jean-Marie Tarascon

► **To cite this version:**

Artem M Abakumov, Stanislav S Fedotov, Evgeny V Antipov, Jean-Marie Tarascon. Solid state chemistry for developing better metal-ion batteries. *Nature Communications*, 2020, 11, pp.4976. 10.1038/s41467-020-18736-7 . hal-03315783

**HAL Id: hal-03315783**





**<https://hal.science/hal-03315783v1>**

Submitted on 5 Aug 2021

**HAL** is a multi-disciplinary open access archive for the deposit and dissemination of scientific research documents, whether they are published or not. The documents may come from teaching and research institutions in France or abroad, or from public or private research centers.

L'archive ouverte pluridisciplinaire **HAL**, est destinée au dépôt et à la diffusion de documents scientifiques de niveau recherche, publiés ou non, émanant des établissements d'enseignement et de recherche français ou étrangers, des laboratoires publics ou privés.

# Solid state chemistry for developing better metal-ion batteries

Artem M. Abakumov <sup>1✉</sup>, Stanislav S. Fedotov <sup>1</sup>, Evgeny V. Antipov <sup>1,2</sup> & Jean-Marie Tarascon <sup>3</sup>

Metal-ion batteries are key enablers in today's transition from fossil fuels to renewable energy for a better planet with ingeniously designed materials being the technology driver. A central question remains how to wisely manipulate atoms to build attractive structural frameworks of better electrodes and electrolytes for the next generation of batteries. This review explains the underlying chemical principles and discusses progresses made in the rational design of electrodes/solid electrolytes by thoroughly exploiting the interplay between composition, crystal structure and electrochemical properties. We highlight the crucial role of advanced diffraction, imaging and spectroscopic characterization techniques coupled with solid state chemistry approaches for improving functionality of battery materials opening emergent directions for further studies.

Invention of new functional materials is vital for the advancement in technologies that will move society towards high global standards of living. Electrode materials have played a crucial role in the development of highly performing Li-ion batteries, as was recognized by the 2019 Nobel Prize recompensing solid-state chemists for their decisive impact<sup>1</sup>. Yet, the vast number of compositions potentially available from the Periodic Table poses an overwhelming challenge for the materials science community to find new battery electrodes. Obviously, researchers desperately need solid guidelines while searching through this huge parameter space for the best chemical combinations and structures. Solid state chemistry is the art of building the desired atomic arrangements based on information hidden in the Periodic Table. Over the decades, this research field has evolved from the trial and error Edison's approach to become a fully-fledged science delivering an unprecedented control over material's structure and properties. This allowed building predictive models and conferring specific functional properties to a material, with an extra degree of freedom offered by defects in solids, structure dimensionality, and nanosizing. Nowadays, the context of research is displaced towards accelerated materials discovery and novel eco-compatible processes together with engineering advances for device fabrication and prototyping. Thus, solid state chemistry is still expanding pursuing our demands of understanding matter and transforming it to useful solids for emerging technologies.

Within the metal-ion battery technology the electrode reactions are based on reversible insertion/deinsertion of the alkali (or alkali-earth) cations  $A^+$  into the host electrode material with a concomitant addition/removal of electrons. In light of this ion-electron duality, it pertains to design an inorganic framework with the proper crystal and electronic structure to reversibly accept and release ions and electrons. This is the favored playground for solid-state chemists

<sup>1</sup>Skoltech Center for Energy Science and Technology, Skolkovo Institute of Science and Technology, Moscow, Russia 121205. <sup>2</sup>Department of Chemistry, Lomonosov Moscow State University, Moscow, Russia 119991. <sup>3</sup>Chimie du Solide-Energie, UMR 8260, Collège de France, 75231 Paris Cedex 05, France. ✉email: [a.abakumov@skoltech.ru](mailto:a.abakumov@skoltech.ru)

willing to better predict and improve battery functionality, as picturized in Fig. 1 with our personal perception of the “composition-structure-property” triad in the context of electrode materials. The specific energy of an insertion material ( $\text{Wh kg}^{-1}$  or  $\text{Wh l}^{-1}$ ) is defined as the product of the operating potential (V) and the capacity ( $\text{Ah kg}^{-1}$  or  $\text{Ah l}^{-1}$ ), both related to the crystal and electronic structure. Extraction of one  $\text{A}^+$  alkali cation is accompanied by loss of one electron which produces both a negatively-charged cationic vacancy and a positively-charged electronic hole in the M–L framework (M—transition metal, L—anion). Generating holes upon battery charge should be considered in the band structure context, but for a chemist it is tempting to link these holes to specific redox centers. Although strongly simplified, this concept enables solid-state chemists to rationalize the electrochemical behavior of electroactive materials on the basis of crystal chemistry, molecular orbitals, ionocovalency, bond valence approach, thermodynamics, and defect chemistry considerations, which provide insights into the electrochemical and thermal stability, charge/discharge mechanisms, structural phase transitions, oxygen evolution, cationic migration and origins of kinetic hindrances.

A legitimate question, however, regards the best way to combine such a chemist’s approach with the spectacular advances in characterization techniques and computational methods so as to be more prolific in identifying practical electrode materials. The design of battery materials has benefited from tremendous progress in computational techniques (first of all, based on density functional theory (DFT) and molecular dynamics (MD)) which greatly contributed to interlinking the “Atoms & Ions” and

“Crystal Structure” sectors in Fig. 1, as reflected in selected reviews<sup>2,3</sup>. Great hopes have been placed in the predictive capabilities of the high-throughput materials genome initiative, being nowadays empowered with artificial intelligence (AI)<sup>4</sup>. The materials genome approach relies on computational electronic structure methods<sup>5</sup> while AI is based on mining, manipulating and reasoning from what is now called Big Data and building artificial neural networks to deduce regularities<sup>6</sup>. So, should our write-up stop here in case of looking old-fashioned? Certainly not. The material-oriented research is still largely driven by simple ideas, hence importance of conceptual models and generalizations. This is what this paper tries to illustrate and discuss as personally perceived.

### Electronic structure and electrochemically induced redox reactions

The redox properties of the insertion materials are best considered in terms of their band structure, which is inherited from the overlapping atomic  $M nd$  orbitals and  $L n/p$  orbitals, as presented in Box 1, panel a, b. Confining to  $L = \text{oxygen}$  for clarity, the relative energy of the  $(M-O)^*$  and  $(M-O)$  bands changes concomitantly with the  $(\Delta-U/2)$  term, where  $\Delta$  and  $U$  are the charge transfer and  $d-d$  Coulomb interaction energies, respectively (Box 1, panel d). High  $\Delta \gg U$  favors the classical insertion reaction associated with the cationic  $M^{(k+1)+}/M^{k+}$  redox couple, in which the relative energy of the  $(M-O)^*$  band with respect to the  $1s$  band in metallic Li governs the electrode redox potential (Box 2), whereas lowering  $\Delta$  increases involvement of the anionic  $O 2p$ -like states (Box 1, panel e). The most practical benefit from

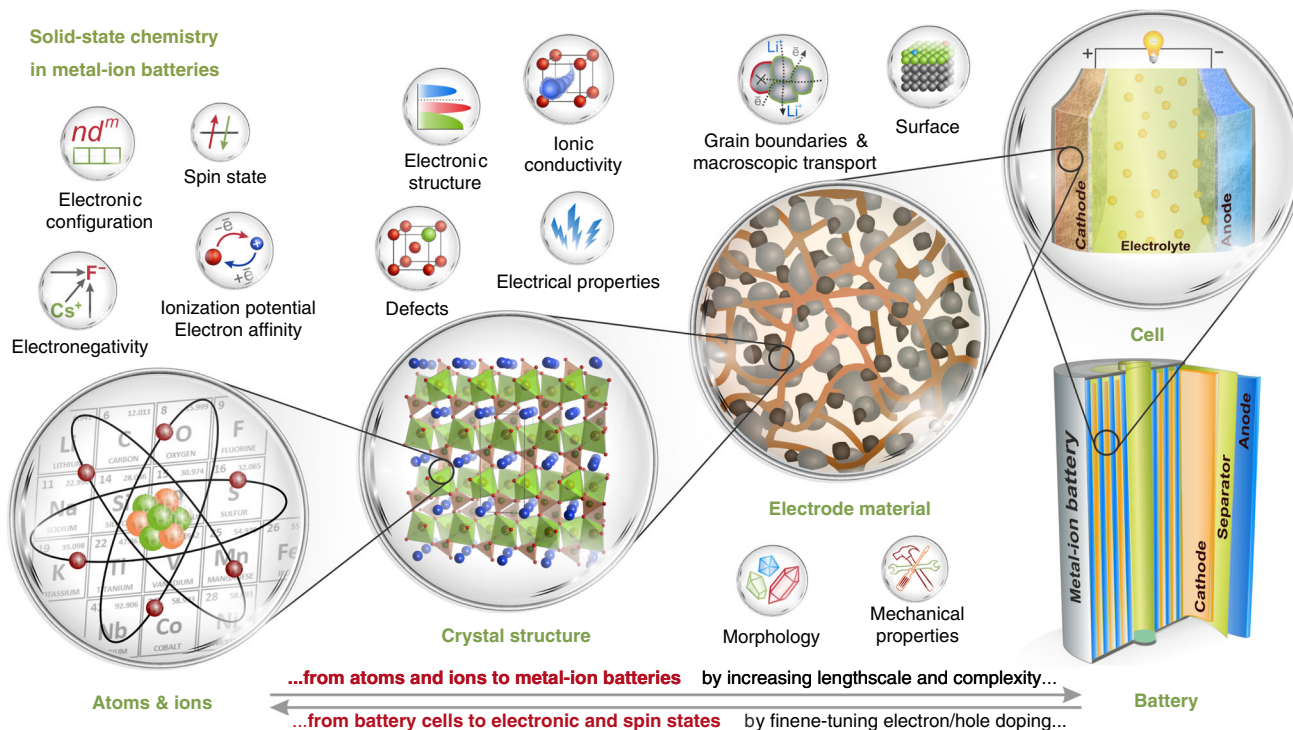
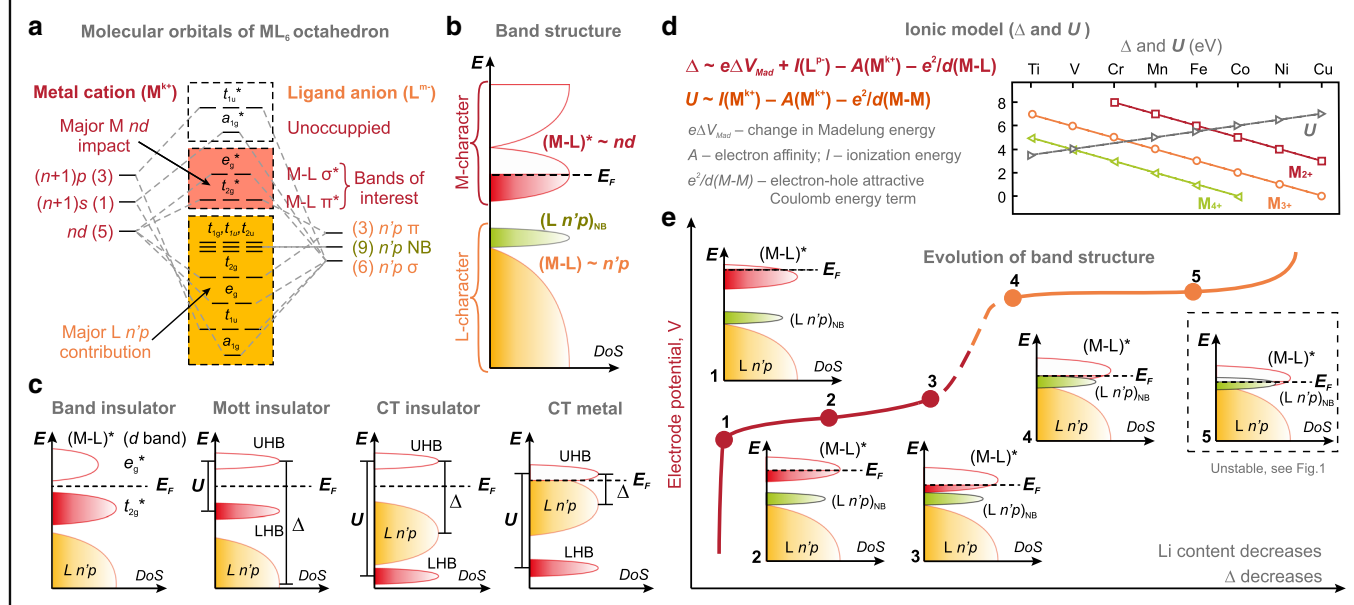


**Fig. 1 The “composition-structure-property” triad in metal-ion batteries.** The individual properties of atoms and ions encoded in the Periodic Table determine the basic redox chemistry, which is fine-tuned by embedding into a certain crystal lattice, in which the peculiar electronic structure and defects define the operating potential, electrochemical capacity, electrochemical stability window, electronic and ionic conductivity. Situated at the next level of complexity, the electrode material combines surface modifications, morphology tuning, and control of grain boundaries optimized for high-energy density, rate capability, and cycling stability through advanced synthesis methods. Further step towards the electrode requires extensive engineering aimed at selecting proper conductive additives and binders and mastering the deposition techniques of the electrode slurry onto current collector. Note that the start and end points of this chain can be reversed, i.e. instead of playing with electronic and crystal structures to design better batteries, one could use the battery as an electrochemical reactor for fine tuning the chemical composition and electronic structure and preparing metastable compounds with unusual oxidation states.

**Box 1 | Molecular orbitals and band theory in application to electrode materials**

In the majority of the insertion compounds for metal-ion batteries a transition metal cation  $M^{k+}$  is octahedrally coordinated with ligands L that results in a schematic band structure deduced from the overlapping atomic M orbitals with L  $n'p$  orbitals (panel a), whereas part of the L  $n'p$  orbitals are not capable of bonding overlap by symmetry and remain non-bonding (NB). The “orbitals of interest”, i.e. those determining the redox properties, comprise the bonding orbitals with a major L contribution (yellow, panel a) and anti-bonding  $e_g$  and  $t_{2g}$  orbitals with a major M  $nd$  impact (pink, panel a). Being placed into a periodic crystal potential, these groups of molecular orbitals give rise to the electronic “bands of interest”, which are the (M-L)\* antibonding and (M-L) bonding bands, and the non-bonding (L  $n'p$ )<sub>NB</sub> band (panel b). However, in case of strong electron-electron correlations one needs to consider the band structure in terms of the Zaanen-Sawatzky-Allen theory<sup>75</sup>. The  $d-d$  Coulomb repulsion splits the partially occupied (M-O)\* band into empty upper and filled lower Hubbard bands (UHB and LHB, respectively) with an energy separation  $U$  that is the energy penalty for  $d^n d^n \rightarrow d^{n+1} d^{n-1}$  electron transfer between adjacent M sites giving rise to a Mott-Hubbard insulator with the bandgap inside the (M-L)\* states (panel c). In case of the large  $U$ , the highest-energy filled band is L  $n'p$ , and virtual electron transfer occurs between ligand and metal, defined by a charge-transfer (CT) energy  $\Delta$ , which is the energy cost of moving an electron from ligand and placing it at the M  $nd$  orbitals  $d^n \rightarrow d^{n+1} L$  (L is the ligand hole). In the Mott-Hubbard regime  $U < \Delta$ , but if  $\Delta < U$ , a CT insulator is realized with the bandgap between the UHB and L  $n'p$  bands.  $\Delta$  and  $U$  can roughly be traced with the ionic model (panel d)<sup>96</sup>. Solid-state chemists manipulate these terms by tuning the electron affinity of the M cations that increases with either their electronegativity or with formal oxidation state. Neglecting electron-electron correlations for the sake of simplification, upon  $Li^+$  removal and in absence of drastic structural transitions, decreasing the Madelung term results in a decrease and increase in energy of the cationic (M-L)\* and anionic L  $n'p$  bands, respectively, hence lowering  $\Delta$ , but the holes still reside in the cationic (M-L)\* band (panel e, points 1-3). Thus, the redox reaction is mostly cationic with the  $M^{k+}$  cation acting as the major redox center. For the  $M^{k+}$  cations with higher electronegativity at the end of the  $M^{(k+1)+}/M^{k+}$  cationic capacity, the L  $n'p$  orbitals are pushed towards the Fermi level equalizing the contributions of the M  $nd$  and L  $n'p$  states (panel e, point 4). The holes equally belong to the cationic and anionic sublattices. The increased hybridization of the M  $nd$  and L  $n'p$  states implies high covalency of the M-L bonding rendering the L ligand a participant of the charge transfer process where holes partially reside at the L  $n'p$  states that, however, does not increase the overall number of electrons donated by the cathode, as the overall number of holes remains the same. Partial oxygen oxidation in contrast can lead to capacity advantages, as realized for the rock-salt based complex transition metal compounds, which by specific structural an stoichiometry reasons ( $L/M$  ratio  $>1$ ) involve redox-active non-bonding (L  $n'p$ )<sub>NB</sub> orbitals<sup>21</sup>. Accordingly, upon  $Li^+$  removal, extra capacity is gained from the localized (L  $n'p$ )<sub>NB</sub> anionic states in addition to that coming from the (M-L)\* band (panel e, point 5).



the anionic redox resides in contribution of non-bonding ( $O 2p$ )<sub>NB</sub> orbitals delivering extra electrons on top of those given by the cationic  $M^{(k+1)+}/M^{k+}$  redox center and, hence, extra capacity. The layered oxides  $Li_{4/3-x}Ni^{2+}_xMn^{4+}_{2/3-x}Co^{3+}_xO_2$  termed “Li-rich NMCs” demonstrate a high reversible capacity exceeding  $250 \text{ mA h g}^{-1}$  that cumulates a cationic redox activity ( $Ni^{2+} \rightarrow Ni^{3+,4+}$  and  $Co^{3+} \rightarrow Co^{4+}$ ) amounting to  $\sim 130 \text{ mA h g}^{-1}$  and an anionic redox activity of  $\sim 120 \text{ mA h g}^{-1}$  at potentials above 4.5 V vs.  $Li^+/Li$ . Pushing the Li removal to its maximum provokes a structural instability of the oxidized oxygen accompanied by the release of  $O_2$ , concomitantly with other practical difficulties, such as sluggish kinetics, voltage fade and hysteresis<sup>7</sup>. Curing this problem calls for a fundamental understanding of the Li-driven anionic redox reactions.

In order to stabilize the highly oxidized oxygen species we need to increase their tightness to the lattice, hence calling for exploration of possible bonding mechanisms. Hong et al.

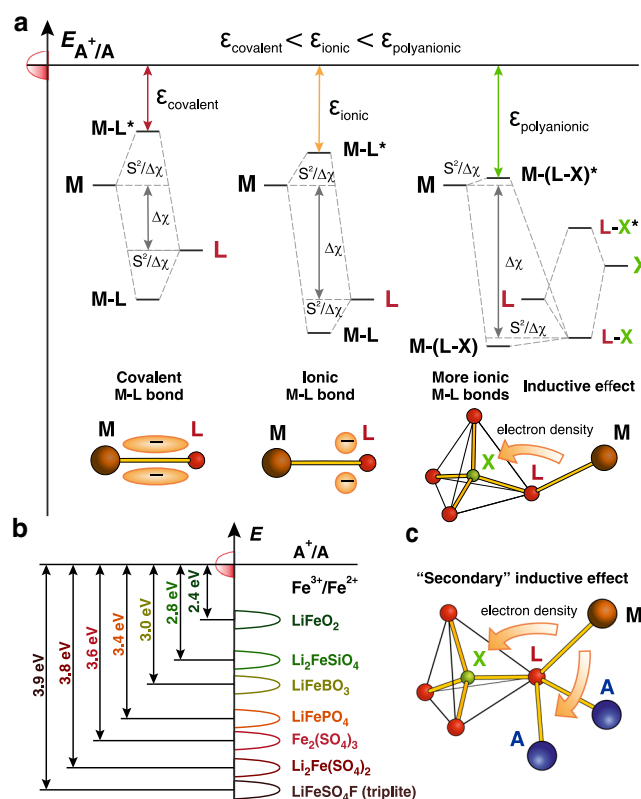
suggested that in Sn-doped  $Li_2IrO_3$  the anionic redox leads to  $\pi$ -bonding between Ir  $5d$  and O  $2p$  orbitals at the cost of shortening the Ir-O interatomic distance to  $<1.8 \text{ \AA}$  (Fig. 2a, left)<sup>8</sup>. However, if  $\pi$ -bonding might look plausible for the  $4d$  and  $5d$  transition metals with diffuse  $d$ -orbitals, it should be less relevant for the  $3d$  transition metals as their rather compact  $d$ -orbitals do not allow for a sufficient  $\pi$ -type overlap with the O  $2p$  orbitals. Alternatively, the oxidized oxygens could provoke the anionic cationation mechanism being linked into the O-O dimers similar to that suggested by J. Rouxel for sulfides<sup>9</sup>. Here, pushing the oxidation of the O  $2p$  non-bonding states implies formation of covalent O-O bonds and corresponding localized  $\sigma$ ,  $\pi$ ,  $\pi^*$ ,  $\sigma^*$  molecular orbitals (Fig. 2a, middle). The holes reside in the high-energy  $\sigma(O-O)^*$ -antibonding orbital pertaining to the  $(O_2)^{n-}$  dimers with short interatomic distance of  $\sim 1.44 \text{ \AA}$  (similar to that in the true  $(O-O)^{2-}$  peroxogroup) bridging two neighboring metal-oxygen octahedra either within the same M-O layer or

**Box 2 | Crystal chemistry rationale behind the operating voltage of metal-ion battery electrodes**

In the general case of M-L (L = ligand) bonding, the electrochemical redox potential is determined by the position of the (M-L)\* band that hosts the Fermi level relative to the Li 1s band. The energy difference between (M-L)\* and (M-L) can be expressed as a function of the overlap integral,  $S^2$ , and electronegativity difference,  $\Delta\chi$ , between M and L (panel **a**). The higher  $\Delta\chi$ , the more ionic the M-L bond. This lowers the  $S^2/\Delta\chi$  and consequently the (M-L)\* band such that the redox potential increases.

Introducing a complex polyanion group  $XL_n^{m-}$  (X = Si, P, S, B, C etc.) offers another degree of freedom in tuning the electrode potential of electrode material by varying ionocovalency of the M-L bonds by means of “inductive effect” (panel **a**, right). In terms of the band structure, placing a highly electronegative X cation lowers the energy of (M-L)\* antibonding states and Fermi level thus enlarging the energy gap between Fermi level in the cathode and the  $Li^+/Li$  redox couple (panel **b**). Further on, the inductive effect is not simply governed by the chemical nature of X: a more accurate prediction of the electrode potential can be made based on the understanding of how the entire coordination environment of the transition metal-ion affects the covalency/ionicity of the M-L bonds including the distances with the nearest neighbors and the contribution of cation-cation electrostatic repulsion<sup>97</sup>. The increased electrostatic repulsion through shorter cation-cation interactions typically results in enlarging of the M-L bond distances and consequently increases their ionicity leading to a higher potential of the  $M^{(k+1)+}/M^{k+}$  redox couple.

At the same time changing the coordination number of the M cation (from  $ML_4$  tetrahedron through  $ML_5$  trigonal bipyramid to  $ML_6$  octahedron) can render the M-L bond more ionic thus raising the  $M^{(k+1)+}/M^{k+}$  redox potential. The number of  $A^+$  alkali cations nesting in a close proximity to the redox center also affects the  $M^{(k+1)+}/M^{k+}$  redox potential that is considered as a “secondary” inductive effect (panel **c**). The A-L bonding increases the ionic character of the M-L bonds through a similar mechanism as to the  $XL_n^{m-}$  polyanions. In practice, shifting the ionocovalency of the M-L bond through the inductive effect appears a useful tool to tune the redox potentials in quite a broad range. For instance, a cumulative inductive effect of fluoride and phosphate anion species in  $KTiPO_4F$  allowed for a substantial boost of the  $Ti^{4+}/Ti^{3+}$  redox potential up to 3.6 V vs.  $K^+/K$  turning it into a prospective cathode despite the well-establish perception of Ti-containing compounds as “only-anode” materials<sup>98</sup>.



between the adjacent M-O layers<sup>10,11</sup>. These peroxogroups are associated with the cationic migration from the M positions to the vacant Li positions leaving “undercoordinated” oxygens which use their 2p orbitals to bind with each other.

In case of the transition metal sulfides, owing to the lower chemical hardness of  $S^{2-}$  with respect to  $O^{2-}$ , the sulfur catenation into disulfide ( $S_2$ )<sup>2-</sup> groups is more pronounced as realized in  $TiS_3 = Ti^{4+}S^{2-}(S_2)^{2-}$  and  $FeS_2 = Fe^{2+}(S_2)^{2-}$ <sup>12,13</sup>. Li insertion is assumed to break the S-S bond resulting in the  $Li_2Ti^{4+}(S^{2-})_3$  and  $Li_2Fe^{2+}(S^{2-})_2$  intercalated structures. However, the long-believed anionic redox intercalation chemistry related to forming/breaking polysulfide S-S bonds still needs a solid crystallographic confirmation. In a broader context, such redox chemistry is recently demonstrated for the low-temperature insertion of Cu into

$La_2O_2S_2$ ,  $Ba_2S_2F_2$ ,  $LaSe_2$ ,  $BaS_2$  containing  $(L_2)^{2-}$  (L = S, Se) dimers to obtain the  $Cu_2La_2O_2S_2$ ,  $Ba_2Cu_2S_2F_2$ ,  $LaCuSe_2$  and  $BaCu_2S_2$  phases<sup>14</sup>. Through this insertion, metallic Cu donates electrons from 3d orbitals to low-lying  $\sigma^*$  orbitals of the  $(L_2)^{2-}$  dimers causing their cleavage. These findings open up a new synthetic strategy worth being explored for designing novel transition metal compounds from precursors containing polyanionic redox centers.

Although the anionic redox scenarios enlisting the M-O  $\pi$ -bonding or the O-O covalent bonding look plausible, they still call for an unequivocal proof of the drastic shortening of the M-O bonds or O-O bonds. Instead, the crystallographic data point to a cooperative deformation of the octahedral framework that was theoretically and experimentally confirmed in both  $\alpha$

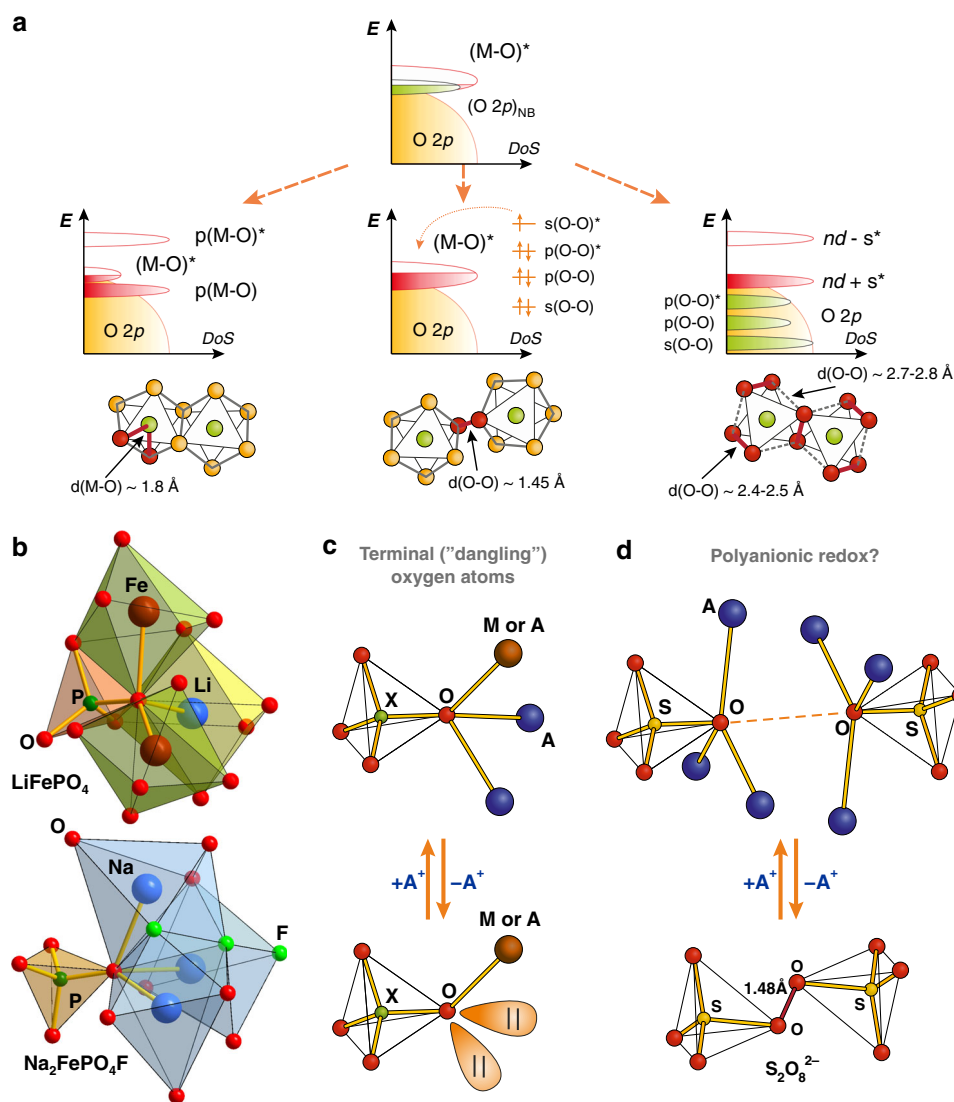


**Fig. 2 Anionic redox in metal-ion battery cathodes.** **a** Stabilization of oxidized oxygen species (from left to right): strengthening of the M-O  $\pi$ -bonds, catenation of oxygens in the  $(\text{O-O})^{2-}$  peroxogroups and cooperative distortion of the anionic framework due to a reductive coupling mechanism.  $sp^3$ -Hybridized oxygen orbitals as lone pairs in the polyanion cathode structures: **b** Local coordination environment of selected oxygens in the  $\text{LiFePO}_4$  and  $\text{Na}_2\text{FePO}_4\text{F}$  structures. **c** Deintercalation of two neighbouring  $\text{A}^+$  alkali cations from the oxo-centered tetrahedron leaves two lone electron pairs residing on the O atom at the center of this tetrahedron. **d** Configuration with two oxo-centered tetrahedra linked to sulfate groups and formation of peroxodisulfate anion  $\text{S}_2\text{O}_8^{2-}$  upon deintercalation of the  $\text{A}^+$  cations.

and  $\beta$ -polymorphs of  $\text{Li}_2\text{IrO}_3$ <sup>15,16</sup>. This deformation, as deduced by transmission electron microscopy and Rietveld refinements, consists in a trigonal prismatic distortion of the  $\text{MO}_6$  octahedra that splits the O-O distances into three long and three short ( $\sim 2.4$ – $2.5$  Å) ones (Fig. 2a, right). Such a shortening of the O-O distances triggers mixing between the partially filled  $\sigma(\text{O-O})^*$ -antibonding orbitals and the  $(\text{M-O})^*$  states resulting in the filled  $nd+\sigma^*$  and empty  $nd-\sigma^*$  bonding and antibonding states, respectively (Fig. 2a, right)<sup>11,17</sup> that is referred to as “reductive coupling”. While a corresponding mechanism has been confirmed for the Li-rich layered oxides of the 4d and 5d transition metals, its occurrence remains questionable for the 3d transition metal oxides as theoretically demonstrated for  $\text{Li}_{2-x}\text{MnO}_3$ <sup>18</sup>, but not impossible. Surprisingly, it was found in the recently discovered pyrite-structured  $\text{FeO}_2$ , which exists at high pressure (76 GPa) and high temperature (1800 K)<sup>19,20</sup>. This suggests that the feasibility of reductive coupling increases with either a spatial extension of the M  $nd$  orbitals, or, otherwise, a shortening of the M-O distances by

applying external pressure. The effect of pressure can be mimicked by epitaxial strain compression in thin films that is known as a tool to modify physical properties. Thus, finding the right epitaxial relations and lattice mismatch could enable stable and reversible oxygen redox due to the reductive coupling in thin film or even 3D electrodes based on 3d transition metal oxides.

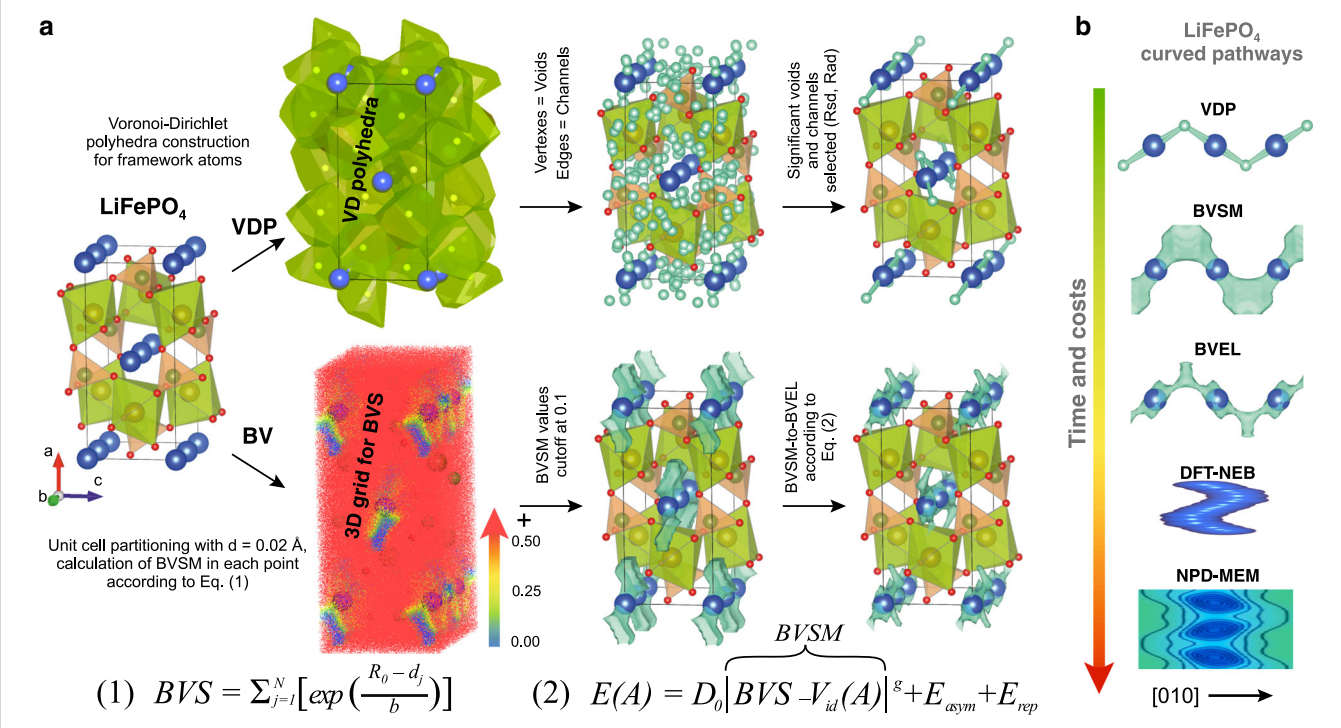
The non-bonding oxygen states in the Li-rich layered oxides are associated with the unhybridized  $(\text{O } 2p)_{\text{NB}}$  orbitals (also called “lone pairs”) aligned along the linear Li-O-Li bridges<sup>21</sup>, but other types of anionic “lone pairs” as electron donors have also been considered in Li-rich layered oxides. This was successfully done in Na-based layered oxides with  $\text{Mg}^{2+}$  and  $\text{Zn}^{2+}$ , which form ionic bonds with oxygen and by the same token can form peroxide compounds ( $\text{MgO}_2$ ,  $\text{ZnO}_2$ )<sup>17,22</sup>. In  $\text{LiFePO}_4$ , the “stellar member” of the polyanionic positive electrode materials, oxygens sit in the oxo-centered tetrahedra (Fig. 2b). Their  $sp^3$  orbitals mix timidly with the Fe 3d states rendering  $\text{LiFePO}_4$  a Mott insulator, but upon delithiation the covalency of the Fe-O bonds increases

**Box 3. | Topology and bond valence approaches to cation diffusion**

Solid-state chemistry methods based on crystal structure analysis can be applied for both electrode and solid electrolyte materials to probe potential ion migration pathways, find intercalation sites, and roughly estimate the activation energy of ion migration within reasonably short time. Among them are purely geometry-topological approaches such as Voronoi-Dirichlet polyhedra (VDP) partition, which deals with crystallographical space, and electrostatics-based methods known as “bond-valence” (BV)<sup>32</sup>.

According to VDP, the crystal space can be split into atoms and voids subspaces. VDPs are built only around so-called “framework” atoms, which remain immobile during ion migration. The vertices and edges of VDP (panel **a**, top) indicate elementary voids and channels sorted by their radii (Rsd, and Rad, respectively). Only significant voids and channels with sufficiently large Rsd and Rad are suitable for mobile ions. Such downselection results in a continuous system represented by curved 1D pathways for LiFePO<sub>4</sub>.

In predominantly ionic and covalent compounds, the sum of bond valences (BVS) of a specific ion should be equal to its valence (formal ionic charge), and can be calculated according to the formula (1), panel **a**, where  $d_j$  is the bond length,  $R_0$  and  $b$  are tabulated constants. The BVS concept is widely recognized as a tool for locating light elements in the structure and identifying mobile ion migration pathways. For this purpose, a BVS value is calculated for each point of a unit cell partitioned into a 3D grid with a given step (<0.2 Å) resulting in a BVS map (panel **a**, middle). The key parameter—BVS mismatch (BVSM)—limits the deviation of all BVS values from the reference (i.e. 1 for Li and other alkali ions). The higher BVSM in a particular area, the lower possibility for a mobile ion to pass through it<sup>99</sup>. Once the sites with low BVSM percolate, ionic conduction is likely to be possible. An important advantage of BVSM is not only low time cost (panel **b**), but also easier treatment of non-stoichiometric compounds (sites with multiple elements or partial occupancies, disorder) by adding corresponding normalizing coefficients to the formula (1). The BVSM values can be translated into energy-related values using a Morse-type interaction potential. Such an approach is called bond valence energy landscape (BVEL)<sup>100</sup>, which is sometimes referred to as bond-valence site energy. With the BVSM input, the site energy,  $E(A)$ , can be estimated according to the formula (2), panel **a**<sup>100</sup>, where  $E_{asym}$ —the energy penalty due to the coordination asymmetry, and  $E_{rep}$ —the electrostatic (Coulomb) repulsion,  $V_{id}$ —expected valence of the A atom,  $D_0$  and  $g$ —empirical coefficients. The BVEL approach might reveal energetically favorable sites for ions or define migration pathways characterized by an activation energy  $E_{act}$ , which can be treated as a migration barrier of a mobile ion. Since BVSM and BVEL deal with a static crystal structure and the relaxation of the surrounding atoms during migration is disregarded, the BVEL migration barrier is generally higher than the experimental one. Nevertheless, substantial literature data for monovalent ions validate a steady correlation between experimental, computational (DFT and MD), and BVEL activation energies. Noteworthy, the solid-state methods also provide a significant gain in time and cost (panel **b**).



converting FePO<sub>4</sub> into a charge transfer insulator with almost pure O 2p states at the Fermi level<sup>23,24</sup>. This electron density forms domains of lone electron pairs (Fig. 2c). Even more interesting are the polyanionic structures exemplified with (but not restricted to) fluoride-phosphates A<sub>2</sub>MPO<sub>4</sub>F (A = Li, Na, M = Fe, Co), within which the tetrahedral oxygens are not even bound to the transition metal; the reasons why they are termed “dangling” or “semilabile” (Fig. 2b)<sup>25,26</sup>. The lone pairs of these oxygens are equivalent to oxygen non-bonding states and could potentially act as electron sources.

Although these electrons are believed to be too low in energy, hope must prevail as evidenced by deintercalation of two Li<sup>+</sup> cations from Li<sub>2</sub>FeSiO<sub>4</sub> apparently assisted by hole formation at

the lone oxygen orbitals<sup>27</sup>. Similar to the anionic redox in oxides, the oxidized oxygen atoms of two neighboring polyanion groups, such as two sulfate groups with the “dangling” oxygens (Fig. 2d), could form a peroxobridge through covalent bonding that is well known as oxidation of sodium hydrogensulfate NaHSO<sub>4</sub> into peroxodisulfate Na<sub>2</sub>S<sub>2</sub>O<sub>8</sub>:  $2\text{SO}_4^{2-} \rightarrow \text{S}_2\text{O}_8^{2-} + 2e^-$ ,  $E^0 = 2.01$  V vs. SHE (estimated as 5.05 V vs. Li<sup>+</sup>/Li). Although the redox potential is beyond the stability window of the standard carbonate-based electrolytes, recent report on highly fluorinated electrolytes stable up to 5.6 V vs. Li/Li<sup>+</sup> might curb this difficulty<sup>28</sup>. In short, it is not therefore impossible to envisage that the polyanionic redox process could be triggered upon removal of Li, hence justifying further exploration.

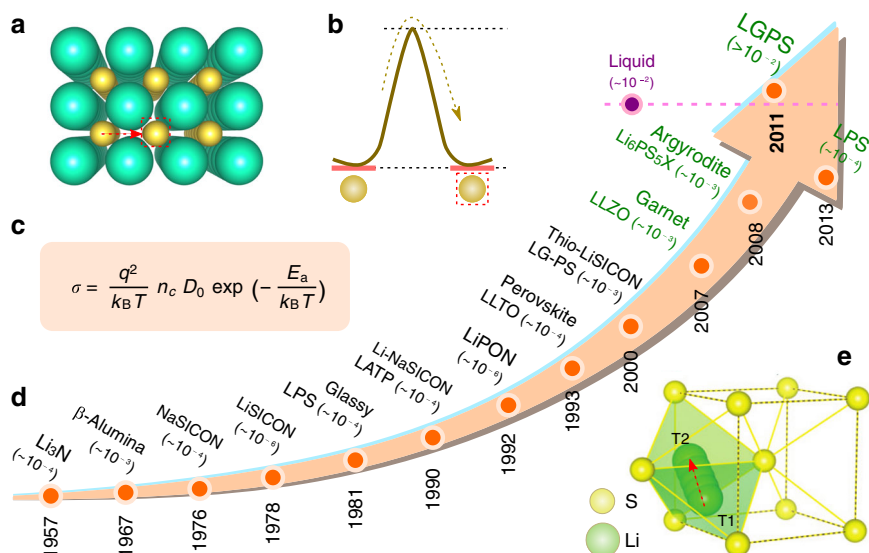


**Fig. 3 Quest for highest Li-ion conductivity in inorganic solids.** The overall equation defining the ionic conductivity  $\sigma$  is shown together with a schematic of the activation energy barrier corresponding to the hopping of ions from site to site within the crystal structure (**a**, **b**) together with the most favorable migration path between two tetrahedral sites  $T_1$  and  $T_2$  in the *b.c.c.* anionic structure (**c**). Development of solid electrolytes over times together with their superionic conductivities (in  $S\cdot\text{cm}^{-1}$ ) indicated in the parentheses (**d**). The legend: NaSiCON:  $\text{Na}_3\text{Zr}_2\text{PSi}_2\text{O}_{12}$ ; LiSiCON:  $\text{Li}_{14}\text{ZnGe}_4\text{O}_{16}$ ; Glassy LPS:  $\text{Li}_2\text{S}-\text{P}_2\text{S}_5$ ; LATP:  $\text{Li}_{1.3}\text{Al}_{0.3}\text{Tl}_{1.7}(\text{PO}_4)_3$ ; LiPON:  $\text{Li}_{2.98}\text{PO}_{3.30}\text{N}_{0.46}$ ; LLTO:  $\text{Li}_x\text{La}_{2/3-x/3}\text{TiO}_3$ ; LG-PS:  $\text{Li}_{4-x}\text{Ge}_{1-x}\text{P}_x\text{S}_4$ ; LLZO:  $\text{Li}_7\text{La}_3\text{Zr}_2\text{O}_{12}$ ; LGPS:  $\text{Li}_{10}\text{GeP}_2\text{S}_{12}$ ; LPS:  $\text{Li}_3\text{PS}_4$ .

One conclusion to be drawn from this brief overview is that, although the general picture of the anionic redox is well established at least with respect to the importance of the O  $2p$  non-bonding states, we are still far from a complete understanding. The main reason is rooted in difficulties of getting precise knowledge on the structure at the end of charge and its evolution during charge-discharge, although the fundamental understanding received from such data is worth the efforts<sup>29</sup>. The structural complexity of layered oxides (abundant stacking faults, cations intermixing, gliding close packed layers upon charge/discharge, cation migration between octahedral/tetrahedral interstices) poses serious obstacles for decent crystallographic studies. Moreover, it is intriguing why there is a relatively small number of extended solids having transition metals coordinated by  $(\text{O}-\text{O})^{2-}$  peroxogroup alike  $\text{WO}_2(\text{O}_2)\text{H}_2\text{O}$ <sup>30</sup> while the panel of materials showing anionic redox activity is rapidly growing? An explanation from a crystal structure and chemical bonding standpoint could really benefit the anionic redox field. Additional insights are also necessary for designing chemical strategies that could help in taking high capacity anionic redox cathodes from the labs into market.

### Ionic transport and defects

So far, considering a battery electrode as an electron reservoir was instructive for establishing a solid connection between the chemical bonding, electronic structure and charge-discharge mechanisms. However, the mobility of the shuttle cations is another important asset for practical implementation of the electrode materials as it largely determines the battery's power. Besides electrode materials, inorganic ionic conductors are becoming of paramount importance for the development of solid-state batteries to meet electric vehicle user's demands for safer and greater autonomy batteries. One of the bottlenecks towards achieving this goal is enhancing ionic conductivity and chemical/electrochemical stability against other battery components<sup>31</sup>. Understanding defect chemistry turns out to be as important as the crystalline matrix to design efficient ionic conductors.

Both battery electrodes and Li(Na)-based inorganic electrolytes can be described as an anionic framework in which mobile cations hop between sites through interconnected diffusion channels. Their ionic conductivity ( $\sigma$ ), which is a thermally activated process following the Arrhenius law, is governed by the charge ( $q$ ), the number ( $n$ ) of mobile carriers (ions, interstitials, vacancies) and the activation hopping energy ( $E_a$ ) for the conducting ion. The latter is the sum of the energies to create the defect and to overcome the energy barrier for the ion migration that depends on the local bonding environment and interconnectivity between available sites in the anionic sublattice. Within a simple ionic model, the electrostatic interactions of neighboring ions together with the free structural volume for ion migration can be estimated fairly well beyond time-consuming DFT-based methods. These approaches, briefly summarized in Box 3, enlist bond valence maps or energy landscapes and crystal space analysis with Voronoi-Dirichlet partitioning<sup>32</sup>. The latter provides the network of diffusion channels and large local spaces promoting fast diffusion. The former delivers a tentative estimate of the energy barriers for ion diffusion, ranking materials by the energetics of this space. The polarizability of the anion sublattice can also be accounted for by appropriate modification of the bond valence parameters<sup>33</sup>. These approaches are typically applied for pre-screening of solid electrolytes and electrode materials being supplemented with simulations of higher accuracy for precise evaluation of the most promising selected examples. As a result, many previously untested compounds with anticipated ion-diffusion properties have been identified as prospective candidates for further investigation not only for the Li-ion conductors, but also for Na-, K-based ones<sup>34-36</sup>.

Trying to identify rules to relate the structure to the ionic conductivity, it has long been recognized that the best ionic conductors ( $\alpha$ -AgI,  $\text{Li}_{10}\text{GeP}_2\text{S}_{12}$ ,  $\text{Li}_7\text{P}_3\text{S}_{11}$ , etc.) have highly polarizable anionic frameworks adopting a body-centered cubic packing (Fig. 3). Such specificity is not fortuitous as recently rationalized by combining a structural matching algorithm with DFT calculations demonstrating that the *b.c.c.* framework allows the  $\text{Li}^+$  ions to migrate through the interconnected tetrahedral



sites with a lower activation barrier compared to *h.c.p.* or *f.c.c.* frameworks<sup>37</sup>. The same trend holds for other monovalent ( $\text{Na}^+$ ) or multivalent ( $\text{Mg}^{2+}$ ) ions. However, since *b.c.c.* anion frameworks are less common than the *h.c.p.* or *f.c.c.* ones, high ionic conductivity should be limited to a small number of compounds. Gladly, there are a few exceptions to the rules with namely the argyrodite-type  $\text{Li}_7\text{PS}_6$  and its halide-substituted derivatives, which show high ionic conductivity while not having a *b.c.c.* anionic framework but still containing tetrahedral sites for the mobile ions. Such insights open perspective for further exploration among both sulfides and oxides.

In the quest for a higher ionic conductivity, lattice stiffness of a few conductors has been monitored by probing the optical and acoustic phonon modes, as well as the phonon density of states via inelastic neutron scattering. Correlating these metrics with the experimental ionic transport reveals that lattice dynamics serves as a useful descriptor for better ionic conductors<sup>38</sup>. Among others, this effect is conveyed in Zn-substituted  $\text{Na}_3\text{PO}_4$  ionic conductors that comprise dynamic rotational disorders in the anionic sublattice enhancing ionic conductivity by the “paddle-wheel” mechanism<sup>39</sup>, where the cation hopping is accompanied by a simultaneous rotation of the anion lowering the activation barrier<sup>40</sup>. A recent study on  $\text{Na}^+$ -ion migration and  $\text{PS}_4^{3-}$  rotation in  $\text{Na}_{11}\text{Sn}_2\text{PS}_{12}$  revealed their intimate coupling and further confirmed the “paddle-wheel” mechanism as a transient opening of a migration window along the  $\text{Na}^+$  transport channels<sup>41</sup>. The “paddle-wheel” mechanism can be intrinsic not only in the crystalline solids with the rotational disorder of the polyanion groups, but also in amorphous solid electrolytes<sup>42</sup>.

Whatever the underlying structure is, it must be recognized that ionic conductivity can also be enhanced with a configurational or occupational disorder resulting from either vacancies or interstitials. Temperature is another elegant way to introduce the configurational disorder, hence explaining why in numerous solid electrolytes the high-temperature (HT) and highly disordered polymorphs always show best ionic conductivity. An illustrative example is the garnet-type  $\text{Li}_7\text{La}_3\text{Zr}_2\text{O}_{12}$  which is tetragonal and a poor ionic conductor at room temperature (RT) ( $\sigma_{\text{RT}} \sim 10^{-6} \text{ S cm}^{-1}$ ) while the HT cubic phase is a good ionic conductor with an extrapolated  $\sigma_{\text{RT}}$  of  $\sim 10^{-4} \text{ S cm}^{-1}$  due to the high Li disorder<sup>43</sup>. Quenching together with chemical substitution are the common strategies to stabilize the HT disordered polymorphs at RT. The highest Li ionic conductivity of  $\sigma_{\text{RT}} \sim 1.4 \times 10^{-3} \text{ S cm}^{-1}$  among oxides was achieved for the inherently disordered Ga-substituted cubic  $\text{Li}_{6.25}\text{Ga}_{0.25}\text{La}_3\text{Zr}_2\text{O}_{12}$  garnet<sup>44</sup> providing the absence of grain boundaries which most frequently negatively affect ionic conductivity. Such boundaries usually originate from crystallites of different orientation in polycrystalline samples and more frequently from minute amounts of surficial phase having either structure, composition or both, different from the grain material.

More spacious and polarizable framework is preferable for ionic conduction, as it weakens the Li-anion bonds reducing  $E_a$ . Along that line, the replacement of  $\text{O}^{2-}$  with larger and more polarizable  $\text{S}^{2-}$  widens the diffusion pathways and improves the conductivity by several orders of magnitude. The research on sulfide-based ionic conductors has recently been accelerated owing to the pioneering work of Kanno *et al* suggesting highly conducting  $(1-x)\text{Li}_4\text{GeS}_4-x\text{Li}_3\text{PS}_4$  phases guided by a tendency of increasing ionic conductivity with the number of mobile charge carriers, namely Li vacancies in the  $\text{Li}_{4-x}\text{Ge}_{1-x}\text{P}_x\text{S}_4$  solid solutions due to the heterovalent  $\text{P}^{5+}$  for  $\text{Ge}^{4+}$  substitution<sup>45</sup>. The actual crystal structure of the  $\text{Li}_{10}\text{GeP}_2\text{S}_{12}$  (or  $\text{Li}_{3.33}\text{Ge}_{0.33}\text{P}_{0.67}\text{S}_4$ ) phase with the highest ionic conductivity  $\sigma_{\text{RT}} \sim 10^{-2} \text{ S cm}^{-1}$  is, however, different from the parent  $\text{Li}_4\text{GeS}_4$  and  $\text{Li}_3\text{PS}_4$  structures<sup>46</sup>. Further optimization via dual cationic (Si for P) and anionic (Cl for S) substitutions resulted in  $\text{Li}_{9.54}\text{Si}_{1.74}\text{P}_{1.44}\text{S}_{11.7}\text{Cl}_{0.3}$

with  $\sigma_{\text{RT}} \sim 2 \times 10^{-2} \text{ S cm}^{-1}$  comparable to that in the Li-based liquid electrolytes<sup>47</sup>. This combination of ligands also provides high ionic conductivities in the argyrodite-type phases  $\text{Li}_6\text{PS}_5\text{X}$  ( $\text{X} = \text{Cl}, \text{Br}, \text{I}$ ) with the maximum  $\sigma_{\text{RT}} \sim 0.94 \times 10^{-2} \text{ S cm}^{-1}$  for  $\text{Li}_{5.5}\text{PS}_{4.5}\text{Cl}_{1.5}$ <sup>48</sup>. Equally, the high temperature  $\beta\text{-Li}_3\text{PS}_4$  polymorph with  $\sigma_{\text{RT}} \sim 10^{-3} \text{ S cm}^{-1}$  can be synthesized at low temperature ( $<150^\circ\text{C}$ ) by nano-structuring via wet-chemical synthesis<sup>49</sup>. However, inherent drawbacks of sulfide-based electrolytes are nested in their limited electrochemical stability which necessitates the use of coatings when placed in contact with oxide positive electrodes, but also in their moisture reactivity which complicates their handling. To alleviate this issue great efforts are placed towards the design of oxysulfides that is a real challenge for solid-state chemists. A viable alternative is provided through revisiting ion transport uncovered back to the 1930's in  $\text{LiX}$  ( $\text{X} = \text{F}, \text{Cl}, \text{Br}, \text{I}$ ) that has led to Li-based ternary halides  $\text{Li}_3\text{YX}_6$  ( $\text{X} = \text{Cl}, \text{Br}$ ) with ionic conductivities of  $0.07\text{--}1.7 \times 10^{-3} \text{ S cm}^{-1}$  after ball milling. Moreover, in terms of practical benefit these ternary halides are stable at high potential as demonstrated with an electrochemically workable ( $\text{Li}_3\text{YCl}_6/\text{LiCoO}_2$ ) cell without pre-coating of the cathode<sup>50</sup>.

At this stage, it is worth recalling that the site energies and migration barriers in the metal-ion battery electrodes may vary upon continuously changing guest cation concentration. Herein, the concentration-dependence of the diffusion activation barriers stems from the size variation of the interstitial voids along the A-cation hopping trajectory due to changing the electronic state of the M cations, their ionic radii and electronically-driven polyhedra distortions. Layered oxide cathodes show many of these aspects that is often accompanied by a short-range migration of the transition metal cations to octahedral positions in the Li layer or to tetrahedral interstices coupled with the anionic redox<sup>29,51</sup>. This migration increases the Li diffusion barriers causing a contraction of the Li layer thickness<sup>52</sup>. Being only partially reversible, the migration gradually transforms the layered structure to spinel-like or disordered rock-salt like structures raising the cell impedance<sup>53</sup>. However, even with a high degree of the Li-M disorder, Li-rich rock-salt oxides can still demonstrate measurable Li diffusion if the Li concentration enables the percolated diffusion paths<sup>54</sup>. The dynamic antisite disorder can equally be induced electrochemically in polyanionic cathode materials possessing the polyanionic groups with “semilabile” oxygen atoms. By extraction of the  $\text{A}^+$  cations these oxygens experience severe underbonding due to the depleted coordination environment (Fig. 2b) that can be partially compensated by migration of the M cation to the vacant A positions<sup>26</sup>. At the same time, the undercoordinated semilabile oxygens with their  $sp^3$  lone electron pairs carry excessive negative charge acting as traps for the  $\text{A}^+$  cations and increasing their hopping barriers<sup>25,55</sup>.

Lastly, the role of the extended defects in ionic transport in solid electrolytes, as mentioned before, is well recognized (particularly the role of grain boundaries), and also acknowledged in the electrode materials. The  $\text{Li}^+$  transport in  $\text{LiCoO}_2$  is demonstrated to be sensitive to diffusivity along the grain boundaries, grain size and spatial distribution of the grains<sup>56</sup>. For instance, a three orders larger diffusion coefficient is expected for  $\text{Li}^+$  ions traveling along the coherent  $\Sigma 2$  grain boundary in  $\text{LiCoO}_2$  compared to that in the direction across the boundary<sup>57</sup>. These examples call for a better understanding of the grain boundary structure and developing advanced chemical approaches to control the grains and grain boundaries in electroactive materials and solid electrolytes.

### Advances in diffraction, imaging and spectroscopic techniques

In spite of a tremendous progress in understanding the metal-ion electrochemical systems conveyed in the previous sections, the

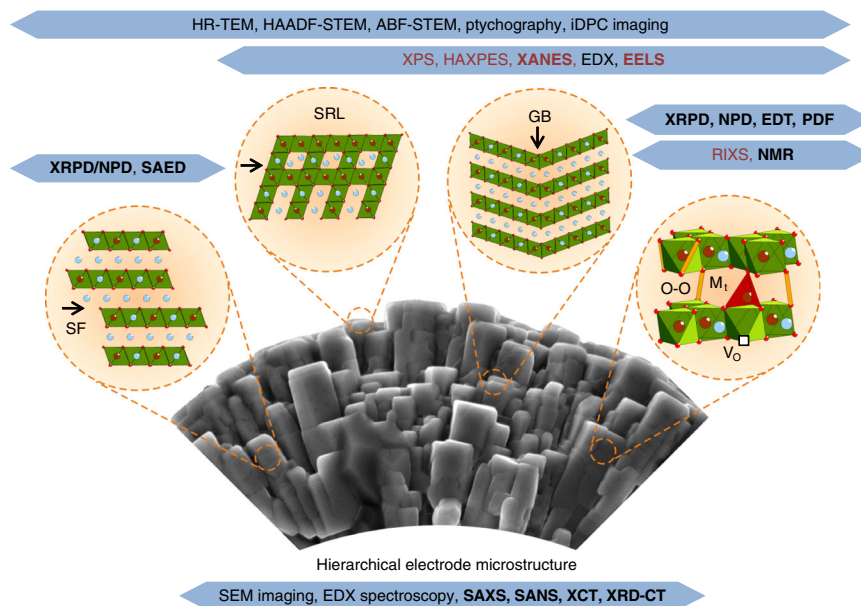


**Fig. 4 Digging into the crystal structure and microstructure of battery electrodes.** Progress in solid state electrochemistry have greatly benefit from establishing robust structural-electronic-electrochemical relationships via the prolific improvement of available diffraction, imaging and spectroscopic characterization techniques and enabling many of them to act in an operando/in situ mode. They target various local structural aspects (vacancies, defects, stacking faults, structure distortions) as well as chemical and electronic aspects. This figure should serve as a guide to the reader for selecting the most suitable type of measurements dealing with a specific problem regarding crystal structure, chemical bonding, electronic structure and composition (as exemplified with the layered rock-salt type oxides). The legend: SF stacking faults; SRL surface reconstruction layer; GB grain boundaries; HR-TEM: high resolution transmission electron microscopy; HAADF-STEM high angle annular dark field scanning transmission electron microscopy; ABF-STEM annular bright field scanning transmission electron microscopy; iDPC integrated differential phase contrast; XPS X-ray photoelectron spectroscopy; HAXPES hard X-ray photoelectron spectroscopy; XANES X-ray absorption near edge structure; EELS electron energy loss spectroscopy; XRPD X-ray powder diffraction; NPD neutron powder diffraction; EDT electron diffraction tomography; SAED selected area electron diffraction; PDF pair distribution function analysis; RIXS resonant inelastic X-ray scattering; NMR: nuclear magnetic resonance spectroscopy; SAXS, SANS: small angle X-ray/neutron scattering; XCT X-ray computed tomography; XRD-CT X-ray diffraction computed tomography. The techniques to probe atomic arrangement are shown in black, those targeting the electronic states and bonding are in red. The techniques in bold can be applied in situ or operando.

extreme complexity of electrodes and solid electrolytes still does not allow retrieving full details on the bulk and defect structures and their evolution upon battery life cycle which too often leads to hypotheses on the exact nature of their electrochemical behavior based on incomplete data. Chemists have at hand powerful diffraction and spectroscopic techniques to interrogate the materials locally and in the bulk (Fig. 4), but we should not miss the advantages offered by the ongoing development of new methods addressing the specific challenges in the metal-ion batteries. A comprehensive overview of the characterization techniques dedicated to fast ionic conductors is available in a recent review<sup>58</sup>, thus we keep focus at the intercalation materials below.

X-ray and neutron powder diffraction (XRPD and NPD) that can be done in either ex situ or in situ modes using dedicated electrochemical cells, enables to determine precisely the crystal structures of electrode materials. An important obstacle pertaining to such techniques is severe distortion of the diffraction intensities and profile shapes by planar defects, such as stacking faults and twins. Li-rich layered oxides  $\text{Li}_{1+x}\text{M}_{1-x}\text{O}_2$  compile such a complexity by reuniting within the same structure faulted stacking associated with random lateral displacements of the “honeycomb” Li/M ordering (Fig. 5a, b), faulted close-packing sequence due to the “cubic-to-hexagonal” transformation of the close-packed layers, and incomplete Li/M ordering depending on the  $x$  value. Although the theory of diffraction from faulted structures is well-known and corresponding software is developed<sup>59</sup>, it is still rarely used, most probably because of the complexity of modeling faulted stacking sequences, but more so owing to their dynamical behavior upon  $\text{Li}^+$  uptake and

removal<sup>60,61</sup>. Tracing the defect structure evolution throughout charge/discharge is still a challenge. Most important, it impedes retrieving precise information on dependence of interatomic distances on the state-of-charge (SoC) limiting our ability to judge on evolution of the chemical bonding. Being sensitive to average long-range order, XRPD and NPD do not probe short-range correlations, and this gap can be closed with total scattering with a pair distribution function (PDF) analysis, which delivers local information on interatomic distances, coordination numbers and disorder, without presuming periodicity<sup>62</sup>. Neutron PDF provides a unique capability to reveal 2D ordering of transition metal cations in the layered oxides and 3D clustering in disordered rock-salt oxides that would be difficult to resolve with other methods because of the closeness of atomic numbers of the  $3d$  transition metals<sup>63</sup>. The local structure can be completed with  $^6\text{Li}$  or  $^{23}\text{Na}$  nuclear magnetic resonance (NMR) spectroscopy which demonstrates high sensitivity towards surrounding of alkali cations by transition metals because of the strong dependence of the hyperfine shift on the number and types of the A-O-M interactions with the paramagnetic centers<sup>64</sup>.

Compared to powder diffraction, electron diffraction tomography (EDT) demonstrates a number of advantages being applied to the Li-ion battery electrode materials<sup>65</sup>. Electron diffraction intensities can be collected ex situ from submicron-sized single crystals of the electrode at different SoCs free of conductive additives and binder interference, and used for the crystal structure solution. The relative sensitivity of EDT to lithium compared to that of X-rays scales as  $\sim [Z_{\text{heavy}}/3]^{1/2}$ , where  $Z_{\text{heavy}}$  is the atomic number of the heaviest element in the structure, hence

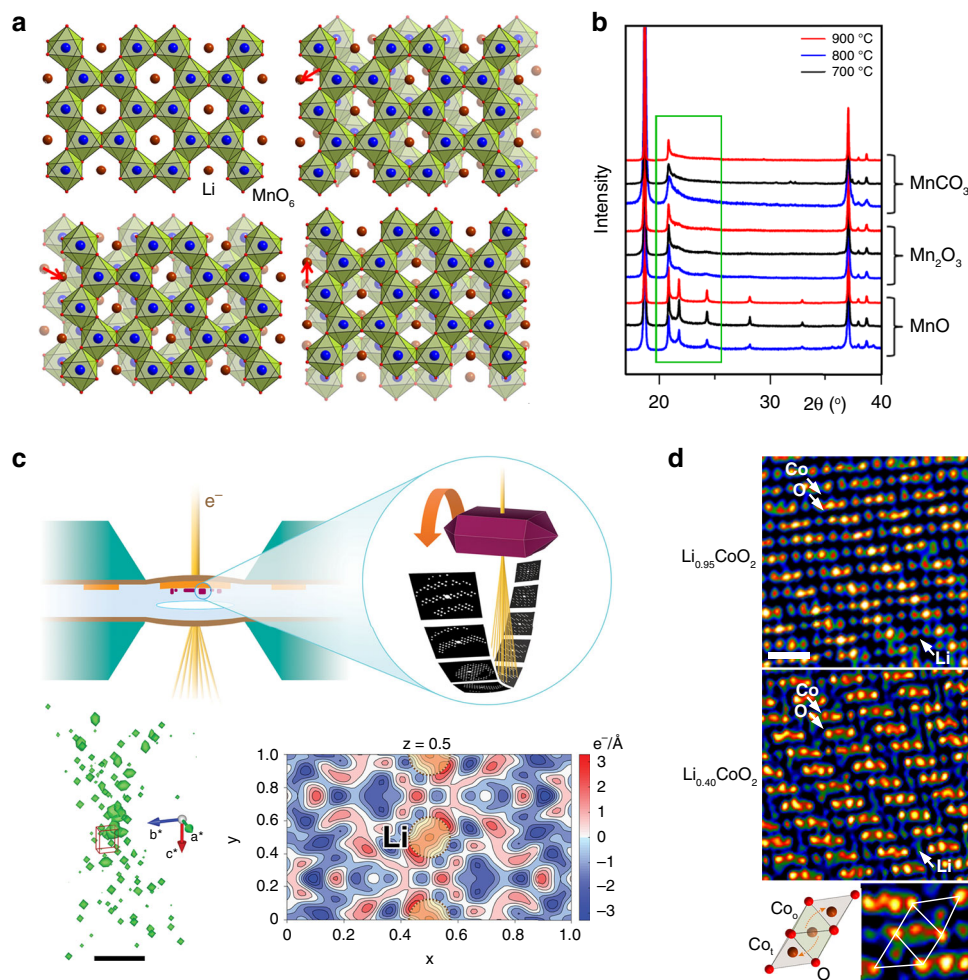


**Fig. 5 Selected advances in crystallographic characterization of the electrode materials.** **a** The structure of “honeycomb”-ordered layers in the Li-rich layered oxides (exemplified with  $\text{Li}_2\text{MnO}_3$ ) and three energetically equivalent lateral displacements of the adjacent layers giving rise to the stacking disorder. **b** Profiles of the reflections in the XRPD pattern of  $\text{Li}_2\text{MnO}_3$  prepared at different temperatures and from different precursors. The profiles of the reflections originating from the “honeycomb” ordering (outlined in green) are affected by stacking faults in various concentrations (reproduced from ref. <sup>61</sup> with permission from the Royal Society of Chemistry). **c** Electron diffraction tomography experiment in a TEM cell with liquid electrolyte and  $\text{Si}_3\text{N}_4$  windows: scheme of the cell and data collection procedure, 3D reciprocal space reconstruction (domains of diffracted intensity at the Bragg positions are shown in green) and difference Fourier map showing the Li positions in the  $\text{LiFePO}_4$  structure. Scale bar is  $5 \text{ nm}^{-1}$  (reproduced from ref. <sup>66</sup> with permission from the American Chemical Society). **d** Projected charge density dDPC maps of  $\text{Li}_{0.95}\text{CoO}_2$  and  $\text{Li}_{0.4}\text{CoO}_2$ : note clear reduction of the charge density at the Li layers. Defects due to migration of the Co atoms from its native octahedral sites ( $\text{Co}_\text{O}$ ) to the tetrahedral interstices ( $\text{Co}_\text{I}$ ) are clearly seen in the enlarged part of the image of the charged  $\text{Li}_{0.4}\text{CoO}_2$  material. Scale bar is 0.5 nm.

enabling a  $\sim 3$  times better Li detection in the structures like  $\text{LiCoO}_2$  and its derivatives. Thus, Li positions, occupancy factors and antisite disorder can be determined rather precisely<sup>26</sup>. Moreover, EDT is so far the only single-crystal diffraction method to retrieve the crystal structure quantitatively from in situ experiments inside the electron microscope using an electrochemical cell with liquid electrolyte (Fig. 5c)<sup>66</sup>. The advantage of EDT relies in the use of a weak electron beam thus reducing electron dose and minimizing electrolyte decomposition. Further advances are rooted in the full dynamical structure refinement that significantly improves the quality of crystallographic data reaching  $\sim 0.02 \text{ \AA}$  precision in atomic positions<sup>67</sup> and in treatment of diffuse electron scattering that provides information on planar defects and disorder<sup>68</sup>.

A deeper insight into the local structure requires advanced transmission electron microscopy (TEM) imaging. Aberration-corrected high angle annular dark field scanning TEM (HAADF-STEM) and annular bright field STEM (ABF-STEM) have extensively been used to visualize the M cation migration upon

the battery cathode cycling<sup>69</sup>, surface layer reconstruction in layered oxides<sup>51</sup>, antisite defects in  $\text{LiFePO}_4$ <sup>70</sup>, O–O dimers formed at anionic redox<sup>15,16</sup>, staged Li-vacancy ordering<sup>71</sup>, and many other local details. However, these techniques require relatively high electron dose to provide images with a reasonable signal-to-noise ratio because the annular detectors used in these methods collect only a small fraction of the electrons interacting with the specimen. Hence, there are risks of creating misleading artefacts for charged cathodes, which are frequently highly instable. Nowadays, a broader availability of fast pixelated or segmented STEM detectors introduced emerging alternative low-dose STEM imaging techniques, such as ptychography and differential phase contrast (DPC). In ptychography, a convergent beam electron diffraction (CBED) pattern is recorded for every scanned point of the specimen with a pixelated electron detector and used for reconstructing an atomic-resolution phase image, which is capable of showing reliably the positions of Li, O and heavier elements even at subpicoampere electron currents<sup>72</sup>. In contrast, during the integrated differential phase contrast

(iDPC-STEM) imaging, the “center of mass” shift of intensity in the CBED pattern at every scanned point is recorded with a 4-quadrant STEM detector. iDPC-STEM retrieves direct phase image of the transmitted electron wave providing a linear dependence of the contrast on the atomic number  $Z$  that is more advantageous for visualizing light elements than the strong  $\sim Z^2$  dependence in the HAADF-STEM imaging<sup>73</sup>. The DPC images can be recorded at the electron dose at least few orders of magnitude lower than a conventional ABF-STEM image still maintaining a good signal-to-noise ratio. As a proof of concept, Fig. 5d shows experimental differential dDPC charge density maps of the LiCoO<sub>2</sub> electrode (5% and 60% delithiated). Spectacularly, Li vacancies are clearly visible already at their low concentration, whereas at large delithiation the Li-vacancy ordering is unambiguously detected, and a partial migration of Co to the tetrahedral interstices becomes apparent.

The low-noise imaging at the low electron dose stands as a serious asset for extracting atomic positions with sub-Å precision through a quantitative image processing with the statistical parameter estimation theory since the highest attainable precision depends on both spatial resolution of the microscope and signal-to-noise ratio of the image. Based on fitting intensity at the atomic columns with Gaussian peaks and retrieving the atomic column positions, this approach has already been applied to a number of materials<sup>74</sup>, and availability of the low-dose STEM imaging techniques makes it a perfect tool to study quantitatively the atomic structures of oxidized oxygen species formed due to the anionic redox, clusters of point defects, grain boundaries and interfaces.

Aside from representing a transformational change in design of high capacity electrode materials, the anionic redox has also modified the characterization landscape calling for new approaches to visualize, besides cations, oxygen atoms and more so to underpin the charge compensation mechanism involving superoxo/peroxo-like (O<sub>2</sub>)<sup>*n*-</sup> species. Hence, a resurgence of interest for spectroscopy techniques, from the time of the high- $T_c$  superconductors, to probe ligand's electronic state as described by the Zaanen-Sawatzky-Allen diagram<sup>75</sup>. Among them, lab X-ray photoelectron spectroscopy (XPS) has been the most popular with its main drawback of probing solely the material surface (<8 nm). However, XPS provided the first hint of anionic activity by the presence of an extra O signal located at 530.5 eV in the O 1s spectrum of Li-rich layered oxides. Its hastily assignment to the (O<sub>2</sub>)<sup>*n*-</sup> species became rapidly controversial because its energy position was structure- and charge-independent<sup>76</sup>. A similar issue occurs with the sulfide compounds showing an anionic redox activity. The same uncertainty remains in hard X-ray photoelectron spectroscopy (HAXPES) which by virtue of a higher energy X-ray beam of ~6.9 keV can increase the inelastic mean free path and therefore the bulk sensitivity up to ~30 nm<sup>77</sup>. To tackle this issue soft X-ray absorption spectroscopy (soft-XAS) which probes the unoccupied states at the atomic level was brought into the scene for looking at the O K-edge. While such a technique demonstrated great merits for cations, a serious pitfall with the O K-edge XAS interpretation is encountered when correlating the intensity changes in the pre-edge of the spectra with the holes on oxygen sites, because of hybridization between the O 2*p* and M levels, hence leading to highly controversial results<sup>78</sup>. Beyond the conventional XAS, resonant inelastic X-ray scattering (RIXS), which probes the excited states promoted by the electric dipole transition, is described as the “Holy Grail” to track the evolution of the M and O redox in Li-rich electrodes upon delithiation. Such a confidence is rooted in the appearance of a specific feature at 523.7 eV emission energy which resonates at 531 eV incident energy<sup>79</sup>. As for HAXPES results, this feature was almost material-neutral and assigned to the anionic redox.

However, no theoretical evidences have allowed to undoubtedly assigning such a feature to the occurrence of exotic O states. Obviously more rigorous implementations of RIXS are being awaited along with an in-depth theoretical support to further elaborate on the nature of the oxidized oxygen species formed during charge and hopefully to bring a corrected trend/picture to this topic.

## Discussion

Modern solid state chemistry, relying on scientific rules, advanced characterization techniques and being empowered with computational tools, is capable of uniting composition, structure and material's properties and delivering predictions by following a deductive reasoning. DFT- and MD-based computational methods provide a valuable insight into different aspects of the electrochemical behavior of battery-related materials. However, they are very demanding for computer power and often offer too simplified treatment of the real chemical systems, such as disordered or partially ordered materials, materials with intersite mixing, high concentrations of defects, strong electron correlations etc. Nevertheless, the predictive power of these methods in battery research have resulted in several experimentally confirmed polyanion electrode materials, such as the A<sub>3</sub>MPO<sub>4</sub>CO<sub>3</sub> (A = Li, Na, M = Fe, Mn) carbonophosphates<sup>80</sup>, LiMoP<sub>2</sub>O<sub>7</sub> pyrophosphates<sup>81,82</sup>, Li<sub>9</sub>V<sub>3</sub>(P<sub>2</sub>O<sub>7</sub>)<sub>3</sub>(PO<sub>4</sub>)<sub>2</sub> phosphate-pyrophosphate<sup>83</sup> and Li<sub>3</sub>Cr<sub>2</sub>(PO<sub>4</sub>)<sub>3</sub><sup>84,85</sup>. However, considering the complexity of the battery materials, a combination of the solid state chemistry approaches with the computational tools still remains serious assets. Among many other examples, this can be illustrated by recent discoveries of metal-ion battery cathodes triggered by the relatively simple concept of the anionic redox and its crystal chemistry expansions: the Li<sub>2</sub>(M,M')O<sub>3</sub> (M = Ru, Ir, M' = Ti, Sn)<sup>15,16,69</sup> and Li<sub>3</sub>IrO<sub>4</sub><sup>86</sup> oxides with the layered and framework structures, the Li-rich disordered xLi<sub>3</sub>NbO<sub>4</sub> - (1-x) LiMO<sub>2</sub> (or Li<sub>2</sub>MO<sub>3</sub>) (M = Mn, Fe, Co, Ni)<sup>87</sup> and short-range ordered Li<sub>1.2</sub>Mn<sub>0.4</sub>M<sub>0.4</sub>O<sub>2</sub> (M = Ti, Zr)<sup>63</sup> rock-salt oxides and Li<sub>1.9</sub>Mn<sub>0.95</sub>O<sub>2.05</sub>F<sub>0.95</sub> oxyfluoride<sup>88</sup>, the Na-based Mg/Zn-doped layered oxides<sup>17,22</sup> and Na-based Li-rich layered oxides<sup>89</sup>, Li<sub>1.68</sub>Mn<sub>0.6</sub>O<sub>4-x</sub>F<sub>x</sub> partially ordered spinels<sup>90</sup>, and, finally, the Li-rich layered Li<sub>1.33-2*y*/3</sub>Ti<sub>0.67-*y*/3</sub>Fe<sub>*y*</sub>S<sub>2</sub> sulfides<sup>91</sup>. However, the next step towards the materials with practical importance is clearly of high demand.

Most likely, methods based on Big Data would come into play in the near future, where the semiquantitative links between the chemical composition, crystal structure and electrochemical properties might form a playground for computer-driven analysis of such relationships. Nowadays we evidence an explosive growth of applications of the machine-learning methods in solid-state materials science aimed at predictions of material's structure and properties<sup>92</sup>. The most significant problem foreseen on this way is the limited size of available well-labeled datasets required for building good models and training the neural networks (that could be mitigated by relying on computational datasets and unsupervised learning algorithms<sup>6</sup>). One could argue that there is a massive amount of data already stored in scientific publications, which are exponentially growing within the field of batteries, but the reported metrics are full of incoherency with respect to composition characterization, preparation techniques, specimen preparation, measurement methods causing the data variance and making a large part of reports obsolete. More importantly, the whole battery research community must be structured to provide standardized and reliable data calling for more “quantitative” experimental characterization techniques, particularly with respect to retrieving information on disorder and defects. Whatever, the predicted materials will have to be synthesized

after all, which brings us back to the skills and competences in solid state chemistry along with some serendipity contribution.

Finally, we have to return back to Fig. 1 and consider it in a reversed perspective, i.e. from the battery to new electronic and spin states and, eventually, new compounds and structures. Battery community has mastered electrochemically-driven intercalation reactions almost to perfection, turning the electrochemical cells into the chemical reactors which enable tuning magnetic, superconducting and catalytic properties<sup>93–95</sup>. Thus the solid-state chemists have received a powerful instrument for precise control of the chemical composition, electron/hole doping and stabilizing metastable compositions and oxidation states.

In summary, with the battery research becoming a society-driven demand, this field attracts a colossal number of researchers having wide ranges of expertise, hence enabling a multifaceted approach. Solid state chemistry should largely help to unite a vision on the many-sided problems of the discovery of novel materials and novel reactivity concepts based on combined experimental and computational methods together with the help of novel advanced characterization techniques with an improved energy and spatial resolution, preferably applied *operando*. To fulfill our prediction and hopes, such a multifaceted platform of knowledge should accelerate the development of better materials for rechargeable batteries.

### Data availability

The raw images associated with Fig. 5d are available from the corresponding author upon reasonable request.

Received: 31 March 2020; Accepted: 10 September 2020;

Published online: 02 October 2020

### References

- Manthiram, A. A reflection on lithium-ion battery cathode chemistry. *Nat. Commun.* **11**, 1550 (2020).
- Urban, A., Seo, D.-H. & Ceder, G. Computational understanding of Li-ion batteries. *npj Comput. Mater.* **2**, 16002 (2016).
- Islam, M. S. & Fisher, C. A. J. Lithium and sodium battery cathode materials: computational insights into voltage, diffusion and nanostructural properties. *Chem. Soc. Rev.* **43**, 185–204 (2014).
- Tabor, D. P. et al. Accelerating the discovery of materials for clean energy in the era of smart automation. *Nat. Rev. Mater.* **3**, 5–20 (2018).
- de Pablo, J. J. et al. New frontiers for the materials genome initiative. *Npj Comput. Mater.* **5**, 41 (2019).
- Gomes, C. P., Selman, B. & Gregoire, J. M. Artificial intelligence for materials discovery. *MRS Bull.* **44**, 538–544 (2019).
- Assat, G. & Tarascon, J.-M. Fundamental understanding and practical challenges of anionic redox activity in Li-ion batteries. *Nat. Energy* **3**, 373–386 (2018). **This seminal review highlights theoretical background, practical realization and limitations of a reversible and stable anionic redox activity in metal-ion battery cathodes.**
- Hong, J. et al. Metal–oxygen decoordination stabilizes anion redox in Li-rich oxides. *Nat. Mater.* **18**, 256–265 (2019).
- Rouxel, J. Anion–cation redox competition and the formation of new compounds in highly covalent systems. *Chem. Eur. J.* **2**, 1053–1059 (1996).
- Xie, Y., Saubanere, M. & Doublet, M.-L. Requirements for reversible extra-capacity in Li-rich layered oxides for Li-ion batteries. *Energy Environ. Sci.* **10**, 266–274 (2017).
- Ben Yahia, M., Vergnet, J., Saubanère, M. & Doublet, M.-L. Unified picture of anionic redox in Li/Na-ion batteries. *Nat. Mater.* **18**, 496–502 (2019). **This work provides a theoretical framework for the unified picture of anionic redox reactions in A-rich transition metal oxides.**
- Furuseth, S., Brattås, L., Kjekshus, A., Andresen, A. F. & Fischer, P. On the Crystal Structures of TiS<sub>3</sub>, ZrS<sub>3</sub>, ZrSe<sub>3</sub>, ZrTe<sub>3</sub>, HfS<sub>3</sub>, and HfSe<sub>3</sub>. *Acta Chem. Scand.* **29a**, 623–631 (1975).
- Brostigen, G. & Kjekshus, A. Redetermined crystal structure of FeS<sub>2</sub> (pyrite). *Acta Chem. Scand.* **23**, 2186–2188 (1969).
- Sasaki, S. et al. A new chemistry route to synthesize layered materials based on the redox reactivity of anionic chalcogen dimers. *Angew. Chem. Int. Ed.* **57**, 13618–13623 (2018).
- McCalla, E. et al. Visualization of O–O peroxo-like dimers in high-capacity layered oxides for Li-ion batteries. *Science* **350**, 1516–1521 (2015). **This work demonstrated a cooperative distortion of the oxygen framework associated with the anionic redox.**
- Pearce, P. E. et al. Evidence for anionic redox activity in a tridimensional-ordered Li-rich positive electrode β-Li<sub>2</sub>IrO<sub>3</sub>. *Nat. Mater.* **16**, 580–587 (2017).
- Vergnet, J., Saubanere, M., Doublet, M.-L. & Tarascon, J.-M. The structural stability of P2-layered na-based electrodes during anionic redox. *Joule* **4**, 1–15 (2020).
- Saubanere, M., McCalla, E., Tarascon, J.-M. & Doublet, M.-L. The intriguing question of anionic redox in high-energy density cathodes for Li-ion batteries. *Energy Environ. Sci.* **9**, 984–991 (2016).
- Hu, Q. et al. FeO<sub>2</sub> and FeOOH under deep lower-mantle conditions and Earth's oxygen–hydrogen cycles. *Nature* **534**, 241–244 (2016).
- Streltsov, S. S., Shorikov, A. O., Skornyakov, S. L., Poteryaev, A. I. & Khomskii, D. I. Unexpected 3+ valence of iron in FeO<sub>2</sub>, a geologically important material lying “in between” oxides and peroxides. *Sci. Rep.* **7**, 13005 (2017).
- Seo, D.-H. et al. The structural and chemical origin of the oxygen redox activity in layered and cation-disordered Li-excess cathode materials. *Nat. Chem.* **8**, 692–697 (2016). **This work uncovered the role of non-bonding oxygen orbitals in the extra capacity delivered by anionic redox.**
- Maitra, U. et al. Oxygen redox chemistry without excess alkali metal ions in Na<sub>2/3</sub>[Mg<sub>0.28</sub>Mn<sub>0.72</sub>]O<sub>2</sub>. *Nat. Chem.* **10**, 288–295 (2018).
- Kou, X.-j., Ke, H., Zhu, C.-b. & Rolfe, P. First-principles study of the chemical bonding and conduction behavior of LiFePO<sub>4</sub>. *Chem. Phys.* **446**, 1–6 (2015).
- Kinyanjui, M. K. et al. Origin of valence and core excitations in LiFePO<sub>4</sub> and FePO<sub>4</sub>. *J. Phys. Condens. Matter* **22**, 275501 (2010).
- Tereshchenko, I. V. et al. The role of semilabile oxygen atoms for intercalation chemistry of the metal-ion battery polyanion cathodes. *J. Am. Chem. Soc.* **140**, 3994–4003 (2018).
- Karakulina, O. M. et al. Antisite disorder and bond valence compensation in Li<sub>2</sub>FePO<sub>4</sub>F cathode for Li-ion batteries. *Chem. Mater.* **28**, 7578–7581 (2016).
- Masese, T. et al. Crystal structural changes and charge compensation mechanism during two lithium extraction/insertion between Li<sub>2</sub>FeSiO<sub>4</sub> and FeSiO<sub>4</sub>. *J. Phys. Chem. C* **119**, 10206–10211 (2015).
- Fan, X. et al. All-temperature batteries enabled by fluorinated electrolytes with non-polar solvents. *Nat. Energy* **4**, 882–890 (2019).
- Yin, W. et al. Structural evolution at the oxidative and reductive limits in the first electrochemical cycle of Li<sub>1.2</sub>Ni<sub>0.13</sub>Mn<sub>0.54</sub>Co<sub>0.13</sub>O<sub>2</sub>. *Nat. Commun.* **11**, 1252 (2020).
- Pecquenard, B. et al. Structure of hydrated tungsten peroxides [WO<sub>2</sub>(O<sub>2</sub>)H<sub>2</sub>O]<sub>n</sub>H<sub>2</sub>O. *Chem. Mater.* **10**, 1882–1888 (1998).
- Famprikis, T., Canepa, P., Dawson, J. A., Saiful Islam, M. & Masquelier, C. Fundamentals of inorganic solid-state electrolytes for batteries. *Nat. Mater.* **18**, 1278–1291 (2019).
- Meutzner, F. et al. Computational analysis and identification of battery materials. *Phys. Sci. Rev.* **4**, 20180044 (2018). **This review demonstrates the geometric and crystal-chemical approaches and methodologies to identify perspective electrochemical energy storage materials.**
- Adams, S. Relationship between bond valence and bond softness of alkali halides and chalcogenides. *Acta Cryst. B* **57**, 278–287 (2001).
- Xiao, R., Li, H. & Chen, L. High-throughput design and optimization of fast lithium ion conductors by the combination of bond-valence method and density functional theory. *Sci. Rep.* **5**, 14227 (2015).
- Eremin, R. A., Kabanova, N. A., Morkhova, Y. A., Golov, A. A. & Blatov, V. A. High-throughput search for potential potassium ion conductors: a combination of geometrical-topological and density functional theory approaches. *Solid State Ion.* **326**, 188–199 (2018).
- Fedotov, S. S. et al. Crystallochemical tools in the search for cathode materials of rechargeable Na-ion batteries and analysis of their transport properties. *Solid State Ion.* **314**, 129–140 (2018).
- Wang, Y. et al. Design principles for solid-state lithium superionic conductors. *Nat. Mater.* **14**, 1026–1031 (2015). **This work reveals a fundamental relationship between anion packing and ionic transport in fast Li-conducting materials.**
- Krauskopf, T. et al. Comparing the Descriptors for Investigating the Influence of Lattice Dynamics on Ionic Transport Using the Superionic Conductor Na<sub>3</sub>PS<sub>4-x</sub>Se<sub>x</sub>. *J. Am. Chem. Soc.* **140**, 14464–14473 (2018).
- Saha, S. et al. Structural polymorphism in Na<sub>4</sub>Zn(PO<sub>4</sub>)<sub>2</sub> driven by rotational order–disorder transitions and the impact of heterovalent substitutions on Na-Ion conductivity. *Inorg. Chem.* **59**, 6528–6540 (2020).
- Jansen, M. Volume effect or paddle-wheel mechanism-fast alkali-metal ionic conduction in solids with rotationally disordered complex anions. *Angew. Chem. Int. Ed.* **30**, 1547–1558 (1991).

41. Zhang, Z., Roy, P.-N., Li, H., Avdeev, M. & Nazar, L. F. Coupled cation–anion dynamics enhances cation mobility in room-temperature superionic solid-state electrolytes. *J. Am. Chem. Soc.* **141**, 19360–19372 (2019).
42. Smith, J. G. & Siegel, D. J. Low-temperature paddlewheel effect in glassy solid electrolytes. *Nat. Commun.* **11**, 1483 (2020).
43. Murugan, R., Thangadurai, V. & Weppner, W. Fast lithium ion conduction in garnet-type  $\text{Li}_7\text{La}_3\text{Zr}_2\text{O}_{12}$ . *Angew. Chem. Int. Ed.* **46**, 7778–7781 (2007).
44. Thangadurai, V., Narayanan, S. & Pinzaru, D. Garnet-type solid-state fast Li ion conductors for Li batteries: critical review. *Chem. Soc. Rev.* **43**, 4714–4727 (2014).
45. Kanno, R. & Murayama, M. Lithium ionic conductor Thio-LISICON: the  $\text{Li}_2\text{S} - \text{GeS}_2 - \text{P}_2\text{S}_5$  system. *J. Electrochem. Soc.* **148**, A742 (2001).
46. Kamaya, N. et al. A lithium superionic conductor. *Nat. Mater.* **10**, 682–686 (2011). **This work demonstrated that high ionic conductivity exceeding that of liquid organic electrolytes can be achieved in non-oxide inorganic solid.**
47. Kato, Y. et al. High-power all-solid-state batteries using sulfide superionic conductors. *Nat. Energy* **1**, 16030 (2016).
48. Adeli, P. et al. Boosting solid-state diffusivity and conductivity in lithium superionic argyrodites by halide substitution. *Angew. Chem., Int. Ed.* **131**, 8773–8778 (2019).
49. Liu, Z. et al. Anomalous high ionic conductivity of nanoporous  $\beta\text{-Li}_3\text{PS}_4$ . *J. Am. Chem. Soc.* **135**, 975–978 (2013).
50. Li, X. et al. Progress and perspectives on halide lithium conductors for all-solid-state lithium batteries. *Energy Environ. Sci.* **13**, 1429–1461 (2020).
51. Pimenta, V. et al. Synthesis of Li-Rich NMC: a comprehensive study. *Chem. Mater.* **29**, 9923–9936 (2017).
52. Kang, K. & Ceder, G. Factors that affect Li mobility in layered lithium transition metal oxides. *Phys. Rev. B* **74**, 094105 (2006).
53. Lin, F. et al. Surface reconstruction and chemical evolution of stoichiometric layered cathode materials for lithium-ion batteries. *Nat. Commun.* **5**, 3529 (2014).
54. Lee, J. et al. Unlocking the potential of cation-disordered oxides for rechargeable lithium batteries. *Science* **343**, 519–522 (2014).
55. Fedotov, S. et al. Crystal structure and Li-ion transport in  $\text{Li}_3\text{CoPO}_4\text{F}$  high-voltage cathode material for Li-ion batteries. *J. Phys. Chem. C* **121**, 3194–3202 (2017).
56. Yamakawa, S., Yamasaki, H., Koyama, T. & Asahi, R. Numerical study of Li diffusion in polycrystalline  $\text{LiCoO}_2$ . *J. Power Sources* **223**, 199–205 (2013).
57. Moriwake, H. et al. First-principles calculations of lithium-ion migration at a coherent grain boundary in a cathode material  $\text{LiCoO}_2$ . *Adv. Mater.* **25**, 618–622 (2013).
58. Gao, Y. et al. Classical and emerging characterization techniques for investigation of ion transport mechanisms in crystalline fast ionic conductors. *Chem. Rev.* **120**, 5954–6008 (2020).
59. Casas-Cabanas, M., Reynaud, M., Rikarte, J., Horbach, P. & Rodriguez-Carvajal, J. FAULTS: a program for refinement of structures with extended defects. *J. Appl. Crystallogr.* **49**, 2259–2269 (2016). **This work introduces a tool for rigorous treatment of powder diffraction patterns from faulted structures.**
60. Shunmugasundaram, R., Arumugam, R. S. & Dahn, J. R. A study of stacking faults and superlattice ordering in some li-rich layered transition metal oxide positive electrode materials. *J. Electrochem. Soc.* **163**, A1394–A1400 (2016).
61. Serrano-Sevillano, J. et al. Enhanced electrochemical performance of Li-rich cathode materials through microstructural control. *Phys. Chem. Chem. Phys.* **20**, 23112–23122 (2018).
62. Mancini, A. & Malavasi, L. Recent advances in the application of total scattering methods to functional materials. *Chem. Commun.* **51**, 16592–16604 (2015).
63. Ji, H. et al. Hidden structural and chemical order controls lithium transport in cation-disordered oxides for rechargeable batteries. *Nat. Commun.* **10**, 592 (2019).
64. Pecher, O., Carretero-González, J., Griffith, K. J. & Grey, C. P. Materials’ methods: NMR in battery research. *Chem. Mater.* **29**, 213–242 (2017).
65. Hadermann, J. & Abakumov, A. M. Structure solution and refinement of metal-ion battery cathode materials using electron diffraction tomography. *Acta Cryst. B* **75**, 485–494 (2019). **This review demonstrates capabilities of quantitative electron crystallography in structural characterization of battery materials.**
66. Karakulina, O. M., Demortière, A., Dachraoui, W., Abakumov, A. M. & Hadermann, J. In situ electron diffraction tomography using a liquid-electrochemical transmission electron microscopy cell for crystal structure determination of cathode materials for li-ion batteries. *Nano Lett.* **18**, 6286–6291 (2018).
67. Palatinus, L., Petříček, V. & Antunes Corrêa, C. Structure refinement using precession electron diffraction tomography and dynamical diffraction: theory and implementation. *Acta Cryst. A* **71**, 235–244 (2015).
68. Mugnaioli, E. & Gorelik, T. E. Structure analysis of materials at the order–disorder borderline using three-dimensional electron diffraction. *Acta Cryst. B* **75**, 550–563 (2019).
69. Sathiyaraj, M. et al. Origin of voltage decay in high-capacity layered oxide electrodes. *Nat. Mater.* **14**, 230–238 (2015).
70. Chung, S.-Y., Choi, S.-Y., Yamamoto, T. & Ikuhara, Y. Atomic-scale visualization of antisite defects in  $\text{LiFePO}_4$ . *Phys. Rev. Lett.* **100**, 125502 (2008).
71. Gu, L. et al. Direct observation of lithium staging in partially delithiated  $\text{LiFePO}_4$  at atomic resolution. *J. Am. Chem. Soc.* **133**, 4661–4663 (2011).
72. Lozano, J. G., Martinez, G. T., Jin, L., Nellist, P. D. & Bruce, P. G. Low-Dose aberration-free imaging of Li-rich cathode materials at various states of charge using electron ptychography. *Nano Lett.* **18**, 6850–6855 (2018).
73. Yücelen, E., Lazić, I. & Bosch, E. G. T. Phase contrast scanning transmission electron microscopy imaging of light and heavy atoms at the limit of contrast and resolution. *Sci. Rep.* **8**, 2676 (2018).
74. Van Aert, S. et al. Advanced electron crystallography through model based imaging. *IUCr* **3**, 71–83 (2016).
75. Zaanen, J., Sawatzky, G. A. & Allen, J. W. Band gaps and electronic structure of transition-metal compounds. *Phys. Rev. Lett.* **55**, 418–421 (1985).
76. Foix, D., Sathiyaraj, M., McCalla, E., Tarascon, J.-M. & Gonbeau, D. X-ray photoemission spectroscopy study of cationic and anionic redox processes in high-capacity Li-ion battery layered-oxide electrodes. *J. Phys. Chem. C* **120**, 862–874 (2016).
77. Assat, G. et al. Fundamental interplay between anionic/cationic redox governing the kinetics and thermodynamics of lithium-rich cathodes. *Nat. Commun.* **8**, 2219 (2017).
78. Yang, W. & Devereaux, T. Anionic and cationic redox and interfaces in batteries: advances from soft X-ray absorption spectroscopy to resonant inelastic scattering. *J. Power Sour.* **389**, 188–197 (2018).
79. Gent, W. E. et al. Coupling between oxygen redox and cation migration explains unusual electrochemistry in lithium-rich layered oxides. *Nat. Commun.* **8**, 2091 (2017).
80. Chen, H. et al. Carbonophosphates: a new family of cathode materials for li-ion batteries identified computationally. *Chem. Mater.* **24**, 2009–2016 (2012).
81. Hautier, G. et al. Designing multielectron lithium-ion phosphate cathodes by mixing transition metals. *Chem. Mater.* **25**, 2064–2074 (2013).
82. Panin, R. V. et al. Pyrophosphates  $\text{AMoP}_2\text{O}_7$  (A = Li and Na): Synthesis, structure and electrochemical properties. *Mater. Res. Bull.* **106**, 170–175 (2018).
83. Jain, A. et al. A computational investigation of  $\text{Li}_9\text{M}_3(\text{P}_2\text{O}_7)_3(\text{PO}_4)_2$  (M = V, Mo) as cathodes for li ion batteries. *J. Electrochem. Soc.* **159**, A622–A633 (2012).
84. Hautier, G. et al. Phosphates as lithium-ion battery cathodes: an evaluation based on high-throughput ab initio calculations. *Chem. Mater.* **23**, 3495–3508 (2011).
85. Herklotz, M. et al. Electrochemical oxidation of trivalent chromium in a phosphate matrix:  $\text{Li}_3\text{Cr}_2(\text{PO}_4)_3$  as cathode material for lithium ion batteries. *Electrochim. Acta* **139**, 356–364 (2014).
86. Perez, A. J. et al. Approaching the limits of cationic and anionic electrochemical activity with the Li-rich layered rocksalt  $\text{Li}_3\text{IrO}_4$ . *Nat. Energy* **2**, 954–962 (2017).
87. Yabuuchi, N. et al. High-capacity electrode materials for rechargeable lithium batteries:  $\text{Li}_3\text{NbO}_4$ -based system with cation-disordered rocksalt structure. *Proc. Natl Acad. Sci. USA* **112**, 7650–7655 (2015).
88. House, R. A. et al. Lithium manganese oxyfluoride as a new cathode material exhibiting oxygen redox. *Energy Environ. Sci.* **11**, 926–932 (2018).
89. House, R. A. et al. Superstructure control of first-cycle voltage hysteresis in oxygen-redox cathodes. *Nature* **577**, 502–508 (2020).
90. Ji, H. et al. Ultrahigh power and energy density in partially ordered lithium-ion cathode materials. *Nat. Energy* **5**, 213–221 (2020).
91. Saha, S. et al. Exploring the bottlenecks of anionic redox in Li-rich layered sulfides. *Nat. Energy* **4**, 977–987 (2019).
92. Schmidt, J., Marques, M. R. G., Botti, S. & Marques, M. A. L. Recent advances and applications of machine learning in solid state materials science. *npj Comput. Mater.* **5**, 83 (2019).
93. Winter, S. M. et al. Models and materials for generalized Kitaev magnetism. *J. Phys.: Condens. Matter* **29**, 493002 (2017).
94. Alekseeva, A. M. et al. New superconductor  $\text{Li}_x\text{Fe}_{1+x}\text{Se}$  ( $x \leq 0.07$ ,  $T_c$  up to 44 K) by an electrochemical route. *Sci. Rep.* **6**, 25624 (2016).
95. Lu, Z. et al. Electrochemical tuning of layered lithium transition metal oxides for improvement of oxygen evolution reaction. *Nat. Commun.* **5**, 4345 (2014).
96. Imada, M., Fujimori, A. & Tokura, Y. Metal-insulator transitions. *Rev. Mod. Phys.* **70**, 1039–1263 (1998).
97. Gutierrez, A., Benedek, N. A. & Manthiram, A. Crystal-chemical guide for understanding redox energy variations of  $\text{M}^{2+/3+}$  couples in polyanion cathodes for lithium-ion batteries. *Chem. Mater.* **25**, 4010–4016 (2013). **This work provides crystal-chemical rationale behind the redox potentials in polyanion cathodes.**
98. Fedotov, S. S. et al. Titanium-based potassium-ion battery positive electrode with extraordinarily high redox potential. *Nat. Commun.* **11**, 1484 (2020).
99. Adams, S. From bond valence maps to energy landscapes for mobile ions in ion-conducting solids. *Solid State Ion.* **177**, 1625–1630 (2006).

100. Adams, S. & Rao, R. P. Transport pathways for mobile ions in disordered solids from the analysis of energy-scaled bond-valence mismatch landscapes. *Phys. Chem. Chem. Phys.* **11**, 3210 (2009).

### Acknowledgements

We thank M-L. Doublet, A. A. Tsirlin, S. Mariyappan, and T. Marchandier for reading the manuscript and valuable comments. J.-M.T. acknowledges funding from the European Research Council (ERC) (FP/2014)/ERC, Grant-Project 670116-ARPEMA. A.M.A. is grateful to Russian Science Foundation for financial support (grant 20-43-01012). Access to the Transmission Electron Microscopy (TEM) facilities was granted by Advanced Imaging Core Facility (AICF) of Skoltech.

### Competing interests

The authors declare no competing interests.

### Additional information

**Correspondence** and requests for materials should be addressed to A.M.A.

**Peer review information** *Nature Communications* thanks the anonymous reviewers for their contribution to the peer review of this work.

**Reprints and permission information** is available at <http://www.nature.com/reprints>

**Publisher's note** Springer Nature remains neutral with regard to jurisdictional claims in published maps and institutional affiliations.



**Open Access** This article is licensed under a Creative Commons Attribution 4.0 International License, which permits use, sharing, adaptation, distribution and reproduction in any medium or format, as long as you give appropriate credit to the original author(s) and the source, provide a link to the Creative Commons license, and indicate if changes were made. The images or other third party material in this article are included in the article's Creative Commons license, unless indicated otherwise in a credit line to the material. If material is not included in the article's Creative Commons license and your intended use is not permitted by statutory regulation or exceeds the permitted use, you will need to obtain permission directly from the copyright holder. To view a copy of this license, visit <http://creativecommons.org/licenses/by/4.0/>.

© The Author(s) 2020